Computational Materials Science 251 (2025) 113773

Contents lists available at ScienceDirect

Computational Materials Science

journal homepage: www.elsevier.com/locate/commatsci

Full Length Article

Advanced machine learning analysis of radiation hardening in reduced-activation ferritic/martensitic steels

Pengxin Wang [a,b], Qing Tao [c], Hongbiao Dong [a], G.M.A.M. El-Fallah [a,*]

[a] School of Engineering, University of Leicester, Leicester LE1 7RH UK
[b] Nanjing Iron & Steel United Co., Ltd., Nanjing 210035 Jiangsu, China
[c] School of Materials and Physics, China University of Mining and Technology, China

ARTICLE INFO

Keywords:
Reduced activation ferritic martensitic (RAFM) steels
Radiation hardening
Machine learning
GBDT
XGBoost
Random forest
Artificial neural network

ABSTRACT

This study uses advanced machine learning models to investigate the radiation hardening behaviour of reduced activation ferritic martensitic (RAFM) steels. An extensive dataset spanning nearly four decades (1985 to 2024) and covering various steel series, including Eurofer97, F82H, T91, OPTIFER, JLM, JLF, and CLAM, was extensively analysed. Multiple models, including Gradient Boosting Decision Trees (GBDT), XGBoost, Random Forests (RF), ResMLP, and One-Dimensional Convolutional Neural Networks (1D-CNN), were employed with hyperparameter optimisation to maximise predictive accuracy. Among these models, GBDT achieved the highest accuracy (R^2: 0.87). The findings reveal significant impacts from elements like Ta, W, and Cr, as well as test temperature and irradiation dose. Radiation hardening peaks at 315 °C due to increased dislocation loops and precipitates but declines above 375 °C as these features diminish and martensitic laths recover, softening the steel. The hardening response to radiation dose shows an increase up to 20 dpa, a slight decrease between 20–35 dpa, and stabilising thereafter. Additionally, W and Cr enhance radiation hardening up to 375 °C, with Cr exhibiting a stronger effect, while Ta is observed to mitigate hardening. These insights contribute to a deeper understanding of radiation effects on RAFM steels, offering a predictive framework for material design and optimisation in nuclear environments. This work highlights machine learning as a powerful tool for advancing materials science and enhancing predictive capability for radiation behaviour in steels.

1. Introduction

Reduced-activation ferritic martensitic (RAFM) steels, known for their excellent mechanical properties, have become key materials for fusion reactors. However, these steels undergo radiation hardening in such environments, significantly affecting their mechanical properties and limiting their service life. Radiation hardening occurs when the internal microstructure of the material changes under high-energy radiation (e.g., neutron irradiation), leading to an increase in strength and brittleness. This phenomenon shortens the operational window of RAFM steels [1–8] with the lower limit of the operating temperature being determined by the peak temperature of radiation hardening.

Research has extensively explored the mechanisms behind radiation hardening in RAFM steels. It was discovered that radiation causes defects such as voids and interstitial atoms [9–11] which hinder dislocation movement and increase steel strength. Additionally, carbides and second-phase precipitates form during irradiation, further obstructing dislocation [12–14]. These carbides have the highest density around 300 °C and gradually decrease at higher temperatures [13] explaining the peak in radiation hardening. Advancements in characterisation techniques also revealed the presence of dislocation loops during irradiation [15–20] which vary in size with irradiation temperature and dose [21–24], disappearing above certain temperatures [25,26].

Despite extensive research, the mechanisms of radiation hardening remain complex and not fully understood. Radiation experiments are time-consuming, costly, and risky [27], leading to insufficient data and hindering a comprehensive understanding of radiation hardening mechanisms. Consequently, researchers have turned to modelling to predict radiation hardening values. Initial models, such as the empirical formula by Dubinko *et al.,* [28] and its refinement by Kotrechko *et al.,* [29] considered factors like dislocation loop density and precipitates but had limitations in applicability. To overcome these challenges, researchers have increasingly turned to simulation-based methods. For instance, Deo et *al.,* [30] used the VPSC model to simulate radiation

* Corresponding author.
E-mail address: gmae2@leicester.ac.uk (G.M.A.M. El-Fallah).

https://doi.org/10.1016/j.commatsci.2025.113773
Received 12 November 2024; Received in revised form 24 January 2025; Accepted 9 February 2025

hardening in ferritic steels, successfully reproducing experimental data. However, the model relies heavily on input parameters such as defect density and size, often derived from limited experimental data. It also assumes uniform defect distributions and does not fully address the coupling between atomic-scale defects and macroscopic properties, limiting its predictive capability. Similarly, Kumar *et al.,* [31] employed a multi-scale approach combining MD and DD simulations to model radiation hardening in Fe-Cr alloys. While this method effectively links nano- and *meso*-scale phenomena, it depends on experimental data for defect characteristics and assumes idealised conditions, such as uniform defect distributions. These limitations and the challenges in multi-scale integration constrain its accuracy and generality. Therefore, a reliable method is needed to analyse and predict radiation-hardening behaviour.

Machine learning (ML), a subset of artificial intelligence, has revolutionised data-driven analysis in materials science. By uncovering intrinsic relationships within complex datasets, ML offers predictive

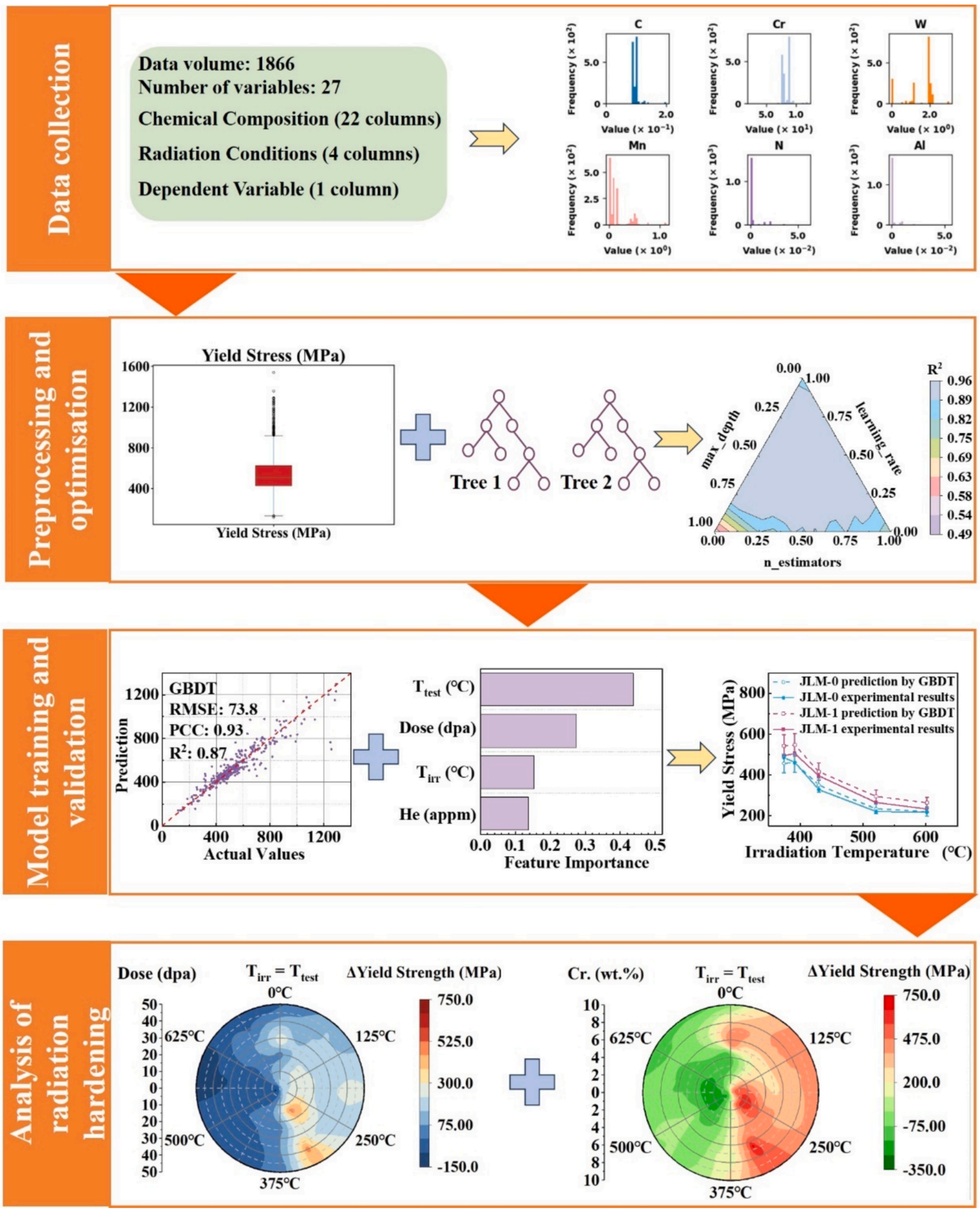

Fig. 1. Flowchart of methodology.

capabilities that are especially useful in scenarios where experimental data are scarce or noisy. Over the past two decades, ML has been successfully applied to various challenges in materials science, including predicting corrosion resistance, optimising additive manufacturing processes, and modelling phase transformations [32–34]. For example, Stewart *et al.,* [35] applied machine learning to predict radiation-induced defect behaviours using regression-based surrogate models. Korotaev *et al.,* [36] used a neural network to predict radiation swelling in austenitic steels, achieving a 1.8 % mean absolute error and aligning well with experimental data. Kemp *et al.,* [37] used an artificial neural network model to predict the radiation hardening, capturing nonlinear dependencies of yield strength on chemical composition and irradiation parameters. However, the model's accuracy was limited. Windsor *et al.,* [38] built on Kemp *et al.*'s work by predicting yield stress at high irradiation levels using simpler neural network models and target-driven dimensionality reduction, achieving good accuracy but still falling short of desired levels for broader applications.

Despite progress, existing models need further refinement in accuracy. Additionally, previous studies mainly focused on overall trends of radiation hardening, without examining the specific effects of different compositions and experimental conditions. This paper addresses these gaps by employing ensemble and neural network-based algorithms, incorporating a unique hyperparameter optimisation method to improve prediction accuracy and mitigate overfitting. Furthermore, we rigorously validated the model to ensure its accuracy and reliability, using it to investigate the differences in radiation hardening among various RAFM steels and explore the impact of different elements on radiation hardening. This study fills a gap in the existing literature, providing new insights for the design and application of RAFM steels in the future.

2. Computational methodology

The methodology is summarised in the flowchart as shown in Fig. 1. A systematic literature review was conducted to compile a dataset of 1866 data points with 27 variables, meticulously constructed from various academic papers and technical reports spanning 1985 to 2024, The dataset, shown in the top section of Fig. 1, includes reduced-activation steels such as Eurofer97, F82H, T91, OPTIFER, JLM, JLF, and CLAM. The variables encompass chemical elements, including Carbon (C), Chromium (Cr), Tungsten (W), Molybdenum (Mo), Tantalum (Ta), Vanadium (V), Silicon (Si), Manganese (Mn), Nitrogen (N), Aluminium (Al), Arsenic (As), Boron (B), Cobalt (Co), Copper (Cu), Oxygen (O), Phosphorus (P), Titanium (Ti), and Zirconium (Zr). Additionally, it includes irradiation conditions such as Irradiation Dose (Dose), Helium Production (He), and Irradiation Temperature (Tirr), along with the corresponding Yield Stress values, Fig. 1, displays the distribution of some of these variables. A detailed description of the dataset and its collection process can be found in the supplementary material under "Data Collection and Description".

The subsequent data cleaning and preprocessing steps involved consolidating the data, handling missing values, detecting and addressing outliers, and standardising the dataset. As shown in the second section of Fig. 1, a boxplot was created, and outliers were removed using the IQR method. Detailed data preprocessing methods can be found in the supplementary material under "Data Preprocessing".

To develop a predictive model for the yield strength of low-activation steels based on their chemical compositions and radiation conditions, we evaluated several machine learning and deep learning models to explore a diverse range of approaches. The tree-based models included Gradient Boosting Decision Trees (GBDT), Random Forest (RF), and XGBoost, which are well-suited for tabular data and are capable of capturing non-linear relationships. GBDT served as the benchmark due to its consistent performance in predictive tasks, while RF and XGBoost provided valuable comparisons with their ensemble learning and regularisation strengths, respectively. In addition, we explored advanced neural network architectures to evaluate their applicability in this domain. The Residual Multi-Layer Perceptron (ResMLP) was chosen for its incorporation of residual connections, which improve gradient flow and enable the training of deeper networks, and layer normalisation, which stabilises training. ResMLP has demonstrated competitive performance on tabular data in recent research [39,40], making it a suitable candidate for this study. Furthermore, a one-dimensional Convolutional Neural Network (1D-CNN) was employed to investigate whether local feature interactions, such as those among alloy compositions and radiation conditions, could enhance predictions. The convolutional layers of the 1D-CNN enable the model to capture such dependencies that may not be evident to tree-based methods.

Following this, for the neural network algorithms (such as ResMLP and 1D-CNN), we use grid search for hyperparameter optimisation due to the complexity and interdependence of their hyperparameters. Grid search allows for a comprehensive exploration of various parameter combinations to identify the optimal configuration. In contrast, for the ensemble algorithms, such as GBDT, XGBoost, and RF, we manually selected the three most critical hyperparameters for each model to optimise the process, thereby avoiding the inefficiencies and overfitting risks associated with automated methods. The contour plot on the left side of the second section in Fig. 1 illustrates the parameter optimisation process using this method. The specific hyperparameter optimisation methods can be found in the supplementary material under the section "Hyperparameter Optimisation". Once the optimal hyperparameters were identified, six models were trained. The trained optimal model was then used to validate experimental results from the literature. We ensured the reliability of this validation through data splitting, model prediction, and performance evaluation. Subsequently, we conducted a feature importance analysis to identify the contribution of each input variable to the prediction of radiation hardening. The third section of Fig. 1 sequentially illustrates the process of model training, feature importance ranking, and model validation.

Finally, based on the model prediction results and the feature importance analysis, we performed a detailed examination of the variables with significant weights to investigate their specific impact mechanisms on radiation hardening. As shown in the final section of Fig. 1, polar coordinate charts were used to visualise the impact of variables on radiation hardening in reduced-activation steels. Through this systematic process, our research aims to comprehensively identify the key factors and mechanisms influencing radiation hardening in RAFM steels. This work provides theoretical support for material design and optimisation.

3. Results and discussion

3.1. Model training and selection

Based on the findings from the Hyperparameter Optimisation section, the optimal hyperparameters were identified and subsequently applied to train the models. During this optimisation process, XGBoost exhibited overfitting on the dataset; therefore, the training was limited to the remaining four models: GBDT, RF, ResMLP, and 1D-CNN. The results are presented in Fig. 2, where (a) shows the GBDT model's predictions, (b) the results of the RF model, (c) the ResMLP model, and (d) the 1D-CNN model.

The scatter plots compare the predictions of Yield Stress (MPa) against the actual values. The red dashed lines represent the range of allowable prediction error, providing a visual measure of how well each model aligns with the actual values. Points falling within the red lines indicate that the predictions are within the acceptable error range, while points outside the red lines reflect greater prediction deviations. This enables a clearer assessment of each model's prediction accuracy and reliability.

For the GBDT model, the predictions align closely with the actual values, indicated by the majority of points falling within the red dashed

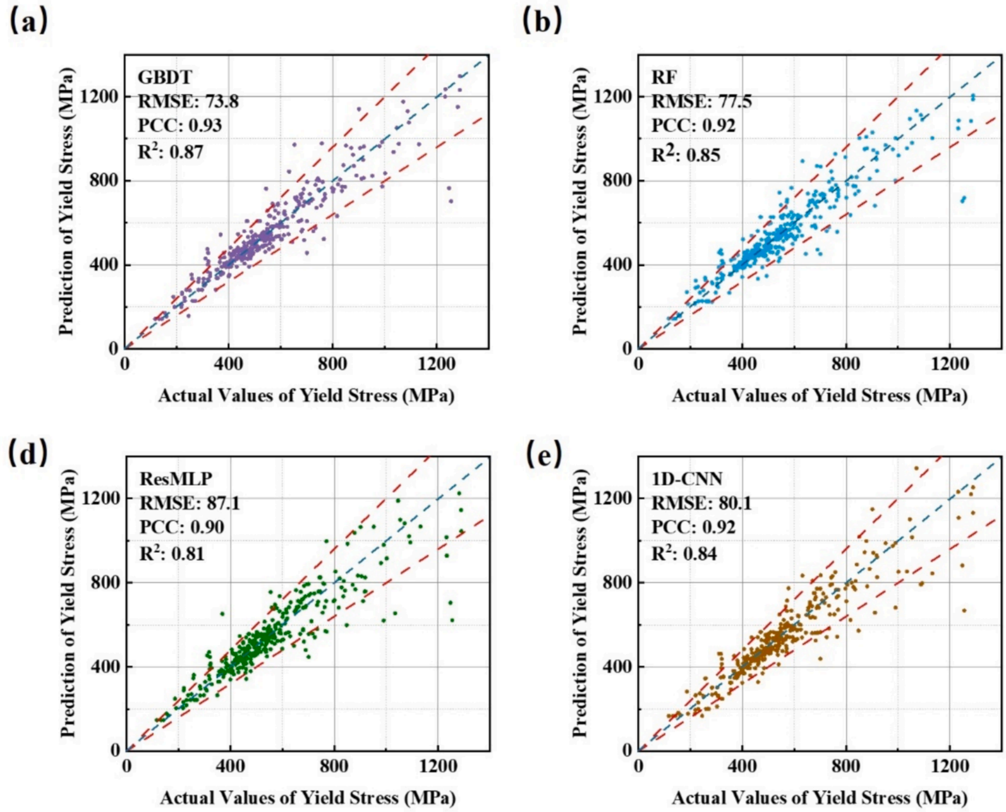

Fig. 2. Comparative scatter plots showing yield stress predictions under radiation conditions for each model.

lines. The model demonstrates strong performance with an RMSE of 73.8, a PCC of 0.93, and an R^2 of 0.87. These metrics reflect a low prediction error, a robust positive correlation, and that 87 % of the variability in Yield Stress is explained by the model. Furthermore, the limited number of points outside the red dashed lines suggests a high degree of reliability in the predictions.

The RF model also shows good alignment, with most points falling within the red dashed lines, though it exhibits a slightly greater scatter compared to the GBDT model. It achieved an RMSE of 77.5, a PCC of 0.92, and an R^2 of 0.85, indicating a low average prediction error and a strong correlation, explaining 85 % of the variability. The few points outside the red dashed lines highlight areas where the model shows minor prediction deviations.

For ResMLP in (c), the results show an RMSE of 87.1, a PCC of 0.90, and an R^2 of 0.81. This indicates better performance than LSTM but still falls short of the GBDT and RF models. A larger number of points are observed outside the red dashed lines, particularly in regions of higher or lower yield stress, indicating that the model has higher variance and less reliability in its predictions compared to the top-performing models.

Finally, the 1D-CNN model, illustrated in (d), performed better than LSTM and ResMLP with an RMSE of 80.1, a PCC of 0.92, and an R^2 of 0.84. The CNN model demonstrates stronger alignment with the actual values, with most points within the red dashed lines, though it shows slightly higher prediction deviations compared to the RF model. This suggests that the 1D-CNN is a robust neural network-based contender, offering results close to the RF model, though not as strong as the GBDT model.

Ultimately, while all models demonstrate strong predictive capabilities, the GBDT model slightly outperforms the RF model, making it the preferred choice for predicting yield stress under radiation-hardening conditions. The 1D-CNN model follows closely behind RF, while ResMLP exhibits higher prediction variance, as evidenced by the larger number of points outside the red dashed lines. The analysis of the red dashed lines reinforces that GBDT provides the most consistent and accurate predictions, followed by RF and 1D-CNN, with ResMLP performing relatively less effectively.

It is worth noting that some points for the GBDT model fall outside the red dashed lines. This is primarily due to the complexity of the collected dataset. The data were gathered from diverse literature sources over an extended period, covering a wide range of steel grades from various regions worldwide. Moreover, the experimental testing for these steels was conducted in different research centres. Specifically, for experiments such as radiation testing, variations between testing centres can significantly influence the results. Consequently, these factors contribute to the presence of data points outside the allowable error range. However, this does not indicate poor model performance. On the contrary, the GBDT model captures the key patterns and features of the data despite its inherent variability, which is further validated in later sections that demonstrate the model's strong performance across validation tests.

3.2. Feature importance analysis

Fig. 3(a) highlights the importance of chemical composition variables on yield stress, determined using the *feature_importances_* attribute of the GBDT model, which was selected based on its superior performance in the model comparison conducted in the previous section. Ta emerges as the most influential element, indicating its significant impact on yield stress. W also shows substantial importance, followed by S, which notably affects yield stress. Cr, Nb, Ni, C, and Si have moderate importance while elements such as V, Al, Mn, and B exhibit lower importance, indicating a relatively minor impact on yield stress.

This distribution of variable importance may differ from general observations due to the specific focus of our study. One key reason is that the target material in this research is low-activation steel, which imposes strict compositional limitations on certain elements [41,42]. As shown

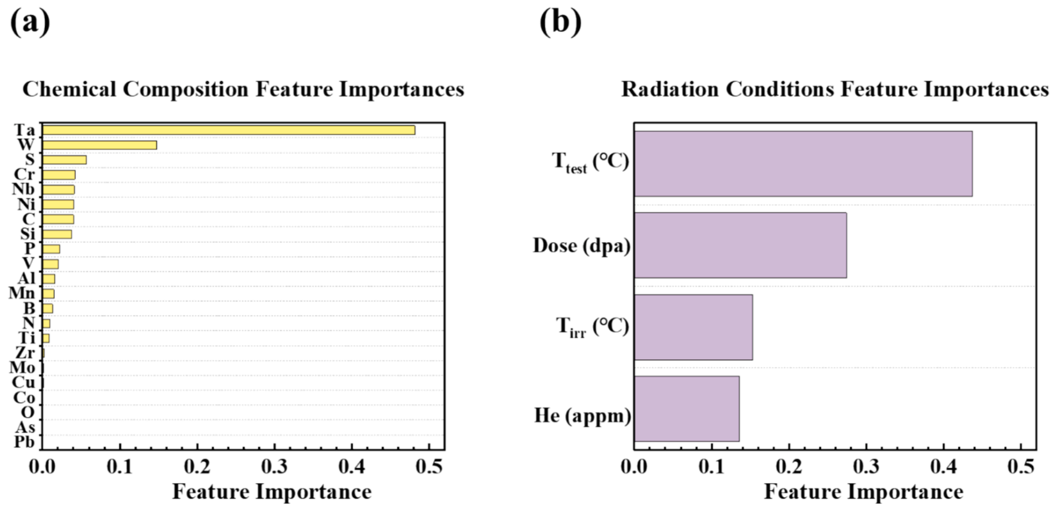

Fig. 3. Variable importance in predicting yield stress under radiation conditions. (a) Chemical composition variables, and (b) radiation condition variables.

in the variable distribution plots in the Supplementary Materials, Nb and B are largely absent in the dataset, and C content is tightly controlled at around 0.1 wt%. These constraints inherently reduce the observed contributions of these elements to yield stress in our model. Another important factor is the scope of this study, which focuses on the effect of chemical composition on yield strength changes under radiation exposure rather than the general strengthening mechanisms in non-irradiated materials.

The results, therefore, reflect the specific compositional constraints and the influence of radiation-induced phenomena rather than conventional strengthening trends. This distinction highlights the importance of considering the material-specific context when interpreting variable importance, particularly for steels designed for specialised environments like radiation exposure.

Fig. 3(b) demonstrates the importance of radiation condition variables on yield stress. T_{test} has the highest importance, significantly impacting yield stress. Irradiation Dose also shows high importance, indicating its notable effect. T_{irr} holds moderate importance, while Helium Content exhibits lower importance but still influences yield stress to some extent.

3.3. Validation of the model

To validate the model, experimental data from the literature were used. The following sections provide a detailed comparison between the GBDT model predictions and experimental results from various studies.

Fig. 4 presents a comparison between the GBDT model predictions and experimental results by A. Kimura [43] for JLM-0 and JLM-1 materials. The x-axis represents Irradiation and test temperatures at 373 °C, 390 °C, 420 °C, 520 °C, and 600 °C, with corresponding doses of 15, 37, 40, 44, and 44 dpa. The y-axis shows yield stress. For JLM-0, the GBDT predictions closely match the experimental data, both showing a decreasing trend in yield stress with increasing temperature. Minor deviations fall within the experimental error margins, validating the model's effectiveness. For JLM-1, the model's predictions also align well with experimental results, though slight discrepancies are observed at higher temperatures.

Fig. 5 presents a comparison between the experimental results by S. Knitel [44] and the GBDT model predictions for both irradiated and unirradiated Eurofer97 steel. The x-axis represents test temperatures ranging from −100 °C to 400 °C, while the y-axis shows yield stress values. The irradiation conditions are specified as 250 °C, 11 dpa, and 540 appm He.

For the irradiated Eurofer97, the experimental results start at approximately 1200 MPa at −100 °C and show a decreasing trend,

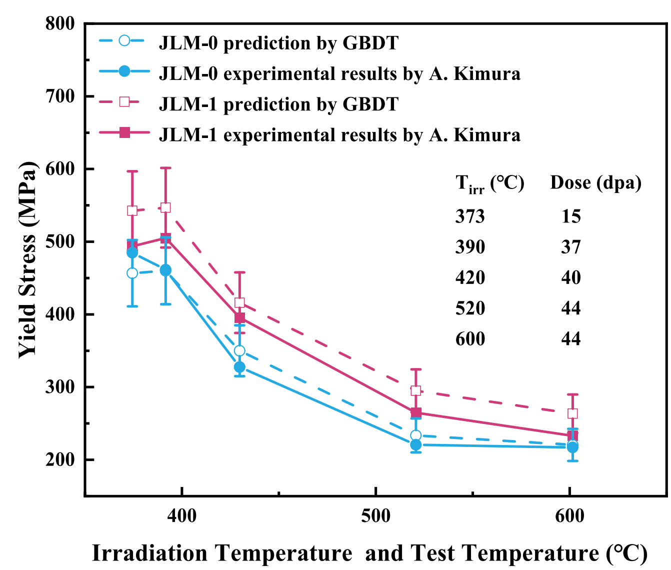

Fig. 4. Comparison of GBDT model predictions and experimental results by A. Kimura [43] for JLM-0 and JLM-1 steels in terms of yield stress against irradiation and test temperatures. The predictions align well with the experimental data.

reaching around 800 MPa at 400 °C. The GBDT model predictions follow a similar trend, starting near 1200 MPa at −100 °C and decreasing to about 880 MPa at 400 °C. Minor deviations between the experimental results and model predictions fall within the experimental error margins.

For unirradiated Eurofer97, the experimental results begin at around 600 MPa at −100 °C and decrease to about 430 MPa at 400 °C. The GBDT model predictions show a close alignment, starting at approximately 600 MPa at −100 °C and decreasing to around 450 MPa at 400 °C. Both the experimental results and GBDT predictions exhibit a decreasing trend in yield stress as the test temperature increases.

Fig. 6 presents a comparison between the experimental results by Kiyoyuki Shiba [45] and the GBDT model predictions for F82H. The irradiation conditions are specified as 250-265 °C, 0.8 dpa, and 100 appm He.

For the F82H, the experimental results start at approximately 820 MPa at 25°C and show a decreasing trend, reaching around 650 MPa at 400 °C. The GBDT model predictions follow a similar trend, starting near

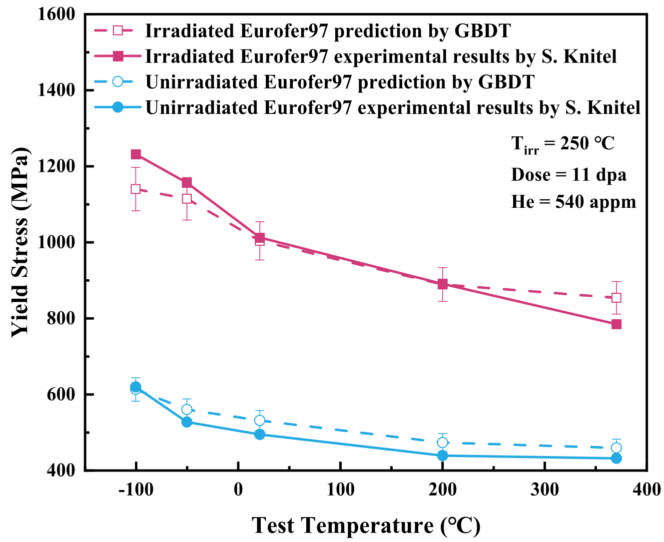

Fig. 5. Comparison of experimental results by S. Knitel [44] and GBDT model predictions for yield stress of irradiated and unirradiated Eurofer97 across test temperatures. The predictions closely match the experimental data.

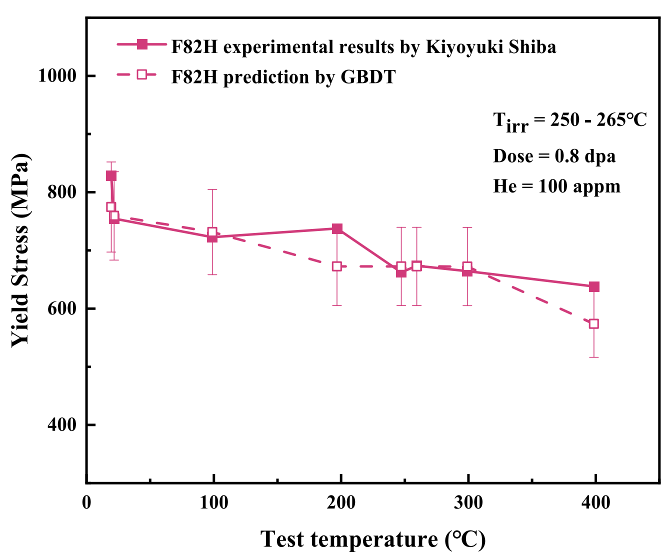

Fig. 6. Comparison of experimental results by Kiyoyuki Shiba [45] and GBDT model predictions for yield Stress of F82H across test temperatures. The GBDT model predictions closely align with the experimental results, demonstrating the model's robust predictability for F82H under the given conditions.

800 MPa at 25°C and decreasing to about 600 MPa at 400 °C. Minor deviations between the experimental results and model predictions are observed, with the experimental data showing slightly higher variability as indicated by the error bars. Despite these deviations, the overall trend in both the experimental results and GBDT predictions is consistent, with yield stress decreasing as the test temperature increases.

Fig. 7 presents a comparison between the GBDT model predictions and experimental results for various steels [46–51]. The x-axis represents the dose ranging from 0 to 80 dpa, while the y-axis shows the change in yield stress. The temperature conditions are specified as 300–335 °C for irradiation and 300–350 °C for testing.

The experimental results for various materials generally demonstrate an increase in ΔYS with dose. For most materials, the increase levels off at higher doses, typically beyond ∼30 dpa. However, some materials, such as Eurofer97 E83698 and E83697 HT, exhibit a continued increase in ΔYS even at higher doses, albeit at a decreasing rate. This behaviour

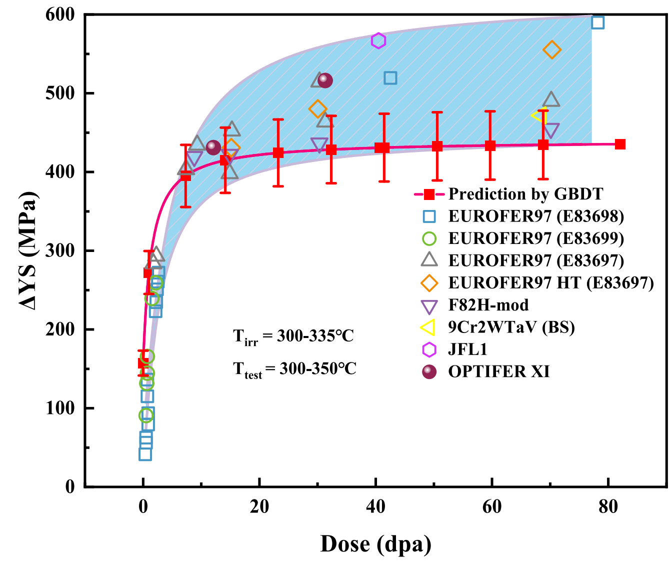

Fig. 7. Comparison of GBDT model predictions and experimental results [46–51] for change in yield stress (ΔYS) against dose (dpa) for various steels. The GBDT model exhibits strong predictive capability, accurately reflecting dose-dependent changes observed in the experimental data.

suggests that, while radiation-induced hardening tends to saturate at higher doses, it does not entirely plateau for these materials. The scatter in the experimental data reflects variability among different materials and experimental conditions. Whilst the predicted trend by GBDT aligns well with the experimental data for Eurofer97 (E83699, E83697) and F82H-mod, certain deviations are observed, particularly at higher doses. Nevertheless, the ΔYS values for most materials converge within the 400–500 MPa range, consistent with the overall trend predicted by the model. Notably, some materials, such as 9Cr2WVTa (BS) and OPTIFER XI, show slightly different behaviours, with ΔYS values either slightly higher or lower than the GBDT predictions. Despite this, the overall agreement between the GBDT model predictions and experimental results is strong, particularly at higher doses where the ΔYS values stabilise.

3.4. Effects of radiation temperature and dose

Based on the validation in the previous section, our model demonstrates high accuracy, enabling us to predict and analyse the effects of radiation temperature and dose on radiation hardening. To intuitively display the relationships between these variables, we use polar coordinate charts to allow for clear observation and facilitate easier analysis of the impact of temperature, and dose, on yield strength.

In these charts: Temperature is represented by the angle, increasing clockwise from 0 °C (top) to 625 °C (bottom). The radiation dose (dpa) is represented by the radius, extending from the centre (0 dpa) to the edge (50 dpa). Yield strength (ΔYield Strength, MPa) is indicated by the colour, ranging from deep blue (lowest) to red (highest), with the colour legend providing specific values.

Fig. 8(a) presents the polar coordinate chart of F82H steel highlighting the significant radiation hardening effect, particularly in the temperature between 125 °C and 375 °C. Yield strength increases significantly as the radiation dose rises from 0 dpa to approximately 20 dpa. Between 20 dpa and 40 dpa, yield strength fluctuates slightly but rises again at 40 dpa, to reach a peak of around 700 MPa at approximately 315 °C.

For Eurofer97 steel, Fig. 8(b), a similar trend is observed, where the radiation hardening effect is notable between 125 °C and 375 °C. As the dose increases from 0 dpa to approximately 20 dpa, yield strength increases significantly. It then shows fluctuations and a slight decrease

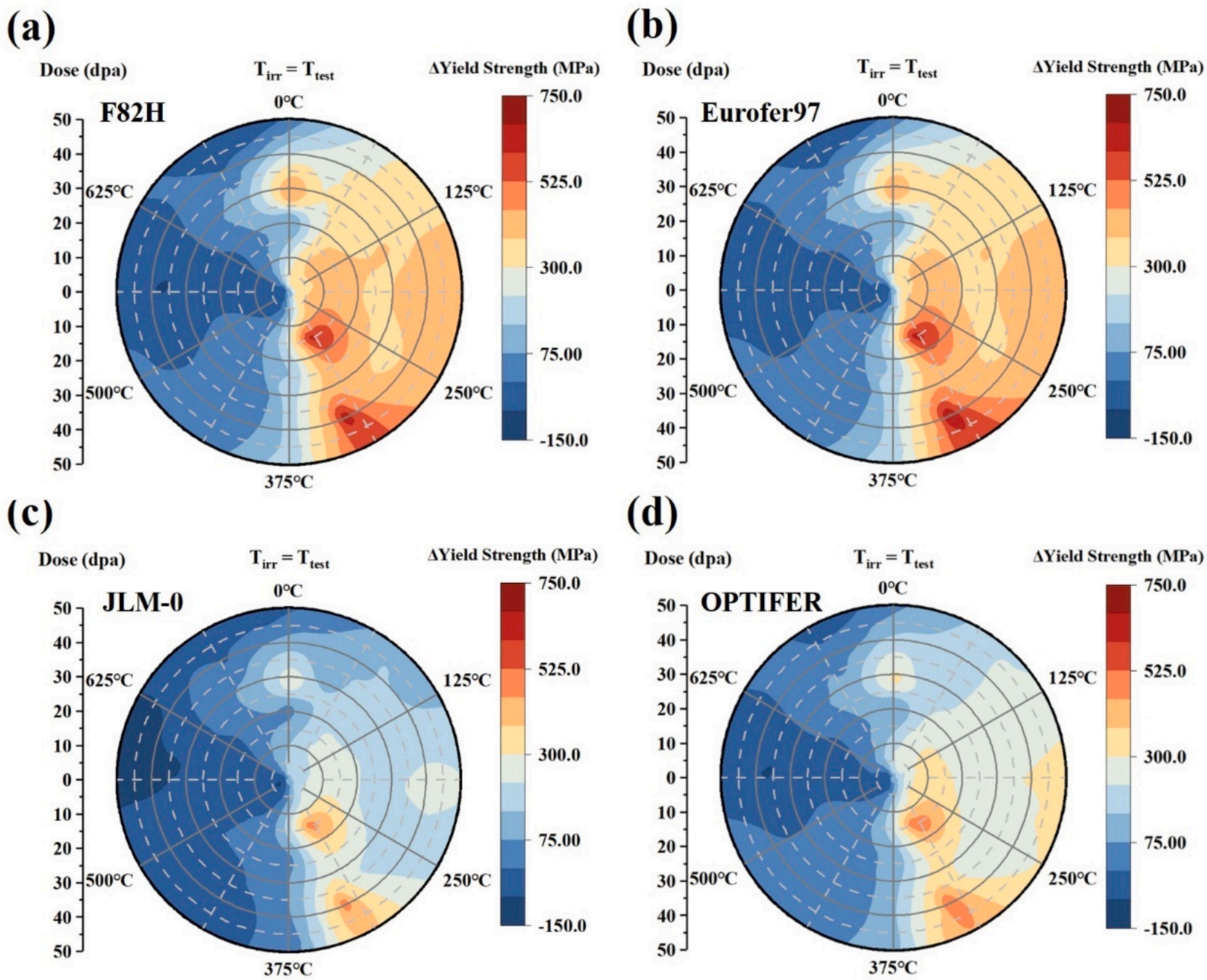

Fig. 8. Polar coordinate charts showing the radiation hardening effects on different steel types as indicated across a range of temperature and radiation doses. Each chart provides a visual representation of the change of yield strength (ΔYS, MPa) with temperature indicated by angle and radiation dose (dpa) by radius.

between 20 dpa and 40 dpa, but rises again at 40 dpa, peaking around 700 MPa at approximately 315 °C.

The chart for JLM-0 steel, Fig. 8(c), indicates a relatively mild radiation hardening effect, mainly between 250 °C and 375 °C. Yield strength increases with the radiation dose from 0 dpa to about 10 dpa. Between 10 dpa and 30 dpa, it fluctuates and slightly decreases, then rises again at 30 dpa, reaching a maximum of approximately 500 MPa around 375 °C.

For OPTIFER steel, in Fig. 8(d), the radiation-hardening effect is similar to JLM-0 steel but slightly more pronounced. Within the 250 °C to 375 °C range, yield strength increases with the radiation dose from 0 dpa to about 20 dpa. It then fluctuates and decreases slightly between 20 dpa and 30 dpa, rising again at 30 dpa, and peaking just below 700 MPa around 315 °C.

The analysis of all the graphs reveals that radiation hardening effects are not uniformly increasing with radiation dose; instead, they exhibit noticeable fluctuations. Generally, the yield strength increases with radiation dose, but there are specific dose ranges where it fluctuates. Kohno *et al.,* [52] conducted radiation dose-dependency tests on JLF series steel, F82H, and HT-9 at 656 ± 700 K. Their results indicated that, with increasing radiation dose, yield strength initially rose to around 15 to 20 dpa before beginning to decline. After reaching 35 dpa, the yield strength slightly increased again, eventually saturating at 40 dpa. Yield strength is likely to peak at around 20 dpa. This is highly consistent with our results, further demonstrating the accuracy of our model.

In the early stages of radiation hardening research, it was generally believed that the phenomenon was due to the formation of dislocation loops. Dubinko *et al.,* [28] proposed a formula for calculating radiation hardening, as shown in Eq. (1). However, their model is not applicable in all cases, as the results in the reference [53] contradict the formula. With further optimisation by Kotrechko *et al.*, [29] it was recognised that the initial model only considered the contribution of dislocation loops to hardening, neglecting the impact of precipitates. Thus, they improved the formula, as shown in Eq. (2) [29]. By combining the above formulas, Eq. (3) was derived [29]. Kotrechko's results have been widely accepted and applied [54–58]. Their experimental results indicated that both the coefficients for the contributions of dislocation loops and radiation precipitates to the overall yield strength (α_{DL} and α_{RP}) are not constant values but vary with radiation temperature, radiation dose, dose rate, and the size and quantity of dislocation loops and precipitates. From their results, many variables influence α_{DL} and α_{RP}, with radiation dose being just one of them. Although studies have shown that an increase in dose can lead to an increase in the number of dislocation loops and precipitates, this is only achievable within a certain temperature range [21]. Therefore, according to Kotrechko's formula, it cannot be confirmed that the degree of radiation hardening increases with the increase in radiation dose. This explains why, within a certain dose range, the degree of radiation hardening does not continuously increase with the radiation dose but instead shows fluctuations.

$$\Delta\sigma_Y = M\alpha Gb\sqrt{N \times d} \tag{1}$$

$$\Delta\sigma_Y = \sqrt{\sigma_{YDL}^2 + \sigma_{YRP}^2} \tag{2}$$

$$\Delta\sigma_Y = MGb\sqrt{\alpha_{DL}^2 N_{DL} \times d_{DL} + \alpha_{RP}^2 N_{RP} \times d_{RP}} \tag{3}$$

where M is the Taylor factor, $N \times d$ is the product of the number density and diameter of the DL's, respectively, G is the shear modulus and b is the Burgers vector. α is the parameter and ranges from 0 to 1. σ_{YDL} and σ_{YRP} represent the yield strengths due to dislocation loops and radiation precipitates, respectively. α_{DL} and α_{RP} are the coefficients for the contributions of dislocation loops and radiation precipitates to the overall yield strength, respectively.

The temperature significantly influences the radiation hardening effect, particularly within the 125 °C to 375 °C range where the hardening effect is most pronounced. At temperatures above 375 °C, the radiation hardening effect diminishes. It can be seen from Fig. 8 that all types of steel reached a peak between 300–350 °C, a phenomenon observed in many previous studies. Many studies [22–25,59,60] observed dislocation loops and precipitates in this temperature range. Specifically, Klimenkov [61] indicated that the number of defects increased rapidly after 300 °C, and this increase in defects hinders the movement of dislocations, thereby enhancing the strength of the steel. Additionally, researchers [22,25,60] also noted that these dislocation loops are significantly time-dependent, with their number peaking between 300–350 °C and then rapidly decreasing. Therefore, the degree of radiation hardening increases with radiation temperature due to the formation of dislocation loops and precipitates. As the temperature rises to 300–350 °C, the density of dislocation loops and precipitates reaches its maximum. With further temperature increase, their density rapidly decreases, accompanied by the recovery of martensitic laths, leading to the softening of the steel. Combining the above results with the descriptions in the relevant literature, it is evident that our model captures the dependence of radiation hardening on radiation temperature accurately.

3.5. Effects of element content

Based on the results of the variable importance analysis, the eight elements with the greatest impact on radiation hardening in terms of chemical composition are Ta, W, S, Cr, Nb, Ni, C and Si. Since S is an element that needs to be controlled during the metallurgical process, and Nb, Ni and Si are radiologically undesired, and because the carbon content in low-activation steels remains relatively stable at around 0.1 %, this study focuses only on the analysis of the effects of Ta, W, and Cr on radiation hardening. Similar to the previous section, polar coordinate charts are used to see the effect of element content on the radiation hardening of Eurofer97. In these charts: Temperature is represented by the angle, increasing clockwise from 0 °C (top) to 625 °C (bottom). Element content (W, Cr, Ta) is represented by the radius, extending from the centre (0 wt%) to the edge (3 wt% for W, 10 wt% for Cr, and 0.6 wt% for Ta). Yield strength (ΔYield Strength, MPa) is indicated by the colour, ranging from deep green (lowest) to red (highest), with the colour legend providing specific values. The radiation dose is set to a fixed value of 50 dpa. The radiation hardening is most pronounced at this dose level, making it ideal for analysing the influence of elements on radiation hardening. Notably, in polar coordinates, Cr content between 0 and 2.25 wt% represents the model's extrapolated results, while the remaining values are within the training dataset and considered interpolated.

Fig. 9(a) shows a polar coordinate chart of W content, highlighting radiation hardening effects from 0 to 3 wt% between 0 °C and 375 °C. The effect is mild from 0 °C to 125 °C but intensifies from 125 °C to 250 °C as W increases from 0 to 2 wt%, then declines between 2 and 3 wt %. From 250 °C to 375 °C, hardening further rises, peaking at around 315 °C, where it reaches approximately 700 MPa at W contents below 0.5 wt% or between 1.5 and 2.5 wt%. Beyond 375 °C, radiation

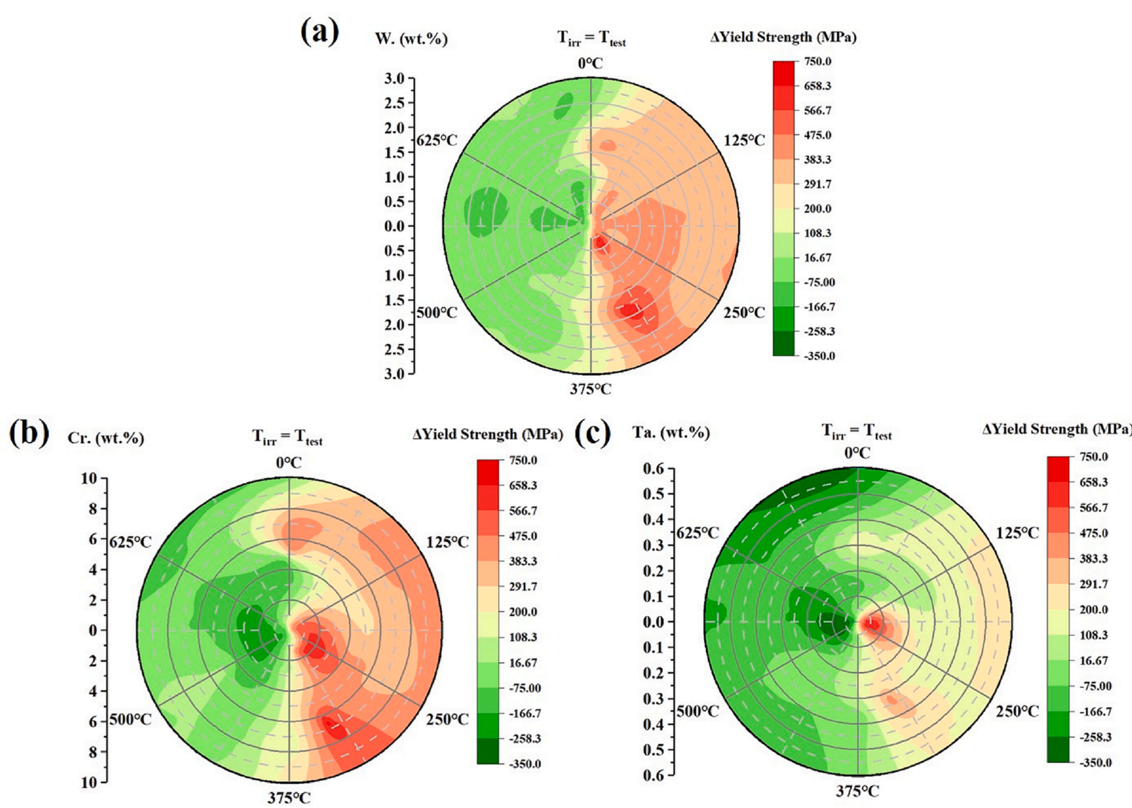

Fig. 9. Effect of alloying element content: (a) W, (b) Cr, and (c) Ta, on radiation hardening in Eurofer97 steels at different temperatures.

hardening declines sharply.

Based on the above results, it can be seen that the addition of W causes significant radiation hardening in steel within the 0-375℃ range, consistent with the findings of many studies [62,63]. W is a high-temperature resistant element, and during irradiation, reduced activation steel precipitates carbides, mainly $M_{23}C_6$ and MX, whereas in $M_{23}C_6$, M primarily represents W, Cr, and Fe [64,65]. Relevant studies have shown that $M_{23}C_6$ does not easily coarsen [66] and is primarily distributed along the grain boundaries of martensitic and ferritic laths, where it stabilises the boundaries during irradiation [67,68], thereby enhancing the strength of the steel. Another study [69] indicated that the stability of $M_{23}C_6$ carbides is enhanced by the addition of tungsten (W). The addition of tungsten increases the driving force for the carbide, making it more stable. Additionally, when tungsten is incorporated into the carbide, the energy barrier for nucleation decreases, making the formation of carbides easier. Due to the low mobility of tungsten in the ferritic matrix, $(Cr, Fe, W)_{23}C_6$ carbides exhibit a lower coarsening rate compared to $(Cr, Fe)_{23}C_6$ carbides. Therefore, the addition of W will make the formation of $M_{23}C_6$ carbides easier, more stable, and less prone to coarsening, which will inevitably further harden the steel under irradiation.

However, as can be seen from Fig. 9(a), the degree of hardening is not directly proportional to the W content. The stability of precipitates under irradiation is a complex process involving competing effects of irradiation-induced ballistic dissolution and radiation-enhanced diffusion [70–74]. Additionally, irradiation-induced solute segregation at the grain boundary further complicates the stability of the precipitates [75]. Therefore, the reason why the degree of radiation hardening is not proportional to the W content may be related to the aforementioned factors. However, due to a lack of related studies, this cannot be confirmed and requires further research.

Fig. 9(b) shows a polar coordinate chart of Cr content, indicating strong radiation hardening across the entire 0 to 10 wt% range from 0 °C to 375 °C, more pronounced than with W. From 0 °C to 125 °C, hardening reaches around 500 MPa at Cr levels of 6 to 8 wt%. As temperatures rise to 125 °C-250 °C, hardening intensifies, peaking near 600 MPa for Cr contents of 0 to 3 wt% while levels of 4 to 8 wt% show lower hardening. From 250 °C to 315 °C, hardening peaks at about 750 MPa at Cr contents of 0 to 0.5 wt% or 6 to 8 wt%. Beyond 375 °C, hardening decreases rapidly.

Similar to the addition of W, the addition of Cr also results in significant radiation hardening of steel within the 0–375 °C range. However, the hardening effect with Cr is more pronounced than with W. The strengthening effect of Cr can be attributed to the precipitation of $M_{23}C_6$ carbides during irradiation, which, as previously discussed, are fine and resistant to coarsening [66], thus enhancing the hardening. Another reason is that Cr is the most abundant element in reduced-activation steel. Studies have shown that as the Cr content increases, the amount of $M_{23}C_6$ in reduced-activation steel also increases [76]. Additionally, Cr is not only present in $M_{23}C_6$. Research indicates that under high radiation doses, high-density (1024 m^{-3}) clusters of approximately 3–5 nm enriched in chromium are observed in the microstructure [77], these clusters impede dislocation movement, further enhancing the hardening effect. This inevitably leads to a greater degree of radiation hardening in steel compared to the addition of W.

Similar to W, we also observe that the degree of radiation hardening is not directly proportional to the Cr content. There is no existing literature indicating this phenomenon, which requires further investigation.

Fig. 9(c) shows a polar coordinate chart of Ta content, revealing significantly lower radiation hardening compared to W and Cr. No substantial hardening occurs from 0 °C to 125 °C. However, at 125 °C-250 °C, hardening increases sharply, peaking near 650 MPa for Ta content between 0 and 0.2 wt%, then decreasing as Ta rises from 0.2 to 0.5 wt%. A slight hardening uptick is seen for Ta between 0.5 and 0.6 wt %. At 250 °C–375 °C, hardening decreases, except for a rise to around 400 MPa at 315 °C for Ta content between 0.3 and 0.4 wt%. Beyond 375 °C, hardening declines rapidly.

Ta is an important component of reduced-activation steel and was ranked first in the previous variable weight sorting. From the polar plot of Ta, it is evident that, unlike W and Cr, the addition of Ta significantly reduces the degree of radiation hardening. In the discussion on W, it was mentioned that the main precipitates in reduced-activation steel are $M_{23}C_6$ and MX, with M being V or Ta, and X being C or N. Research [71] has shown that during irradiation, there is a phenomenon of re-solution of TaC in reduced-activation steel. This has been explained by radiation-induced amorphisation and radiation-enhanced diffusion at the given temperature range. This explains why steels with low Ta content exhibit significant hardening between 125–250 °C, while above 250 °C, due to radiation-induced amorphisation and radiation-enhanced diffusion, TaC disappears, thereby reducing its pinning effect on dislocations and consequently decreasing the hardening degree. Furthermore, studies [78] have indicated that the addition of Ta accelerates the recovery of martensite during irradiation, which also reduces the radiation hardening of steel. Therefore, the addition of Ta lowers the degree of radiation hardening.

4. Conclusion

In this study, we analysed radiation hardening data from 1985 to 2024, covering a range of steel types including Eurofer97, F82H, T91, OPTIFER, JLM, JLF, and CLAM. We used GBDT, XGBoost, RF, ResMLP, and 1D-CNN for modelling the data. Following extensive data preprocessing and hyperparameter optimisation, we assessed the models' performance. The most accurate model was then selected and its predictions were compared with experimental data from the literature for validation. Finally, we used this model to predict and examine the effects of chemical composition and radiation conditions on radiation hardening in reduced activation steels. Our key findings are as follows:

1. **Model Performance:** Hyperparameter optimisation indicated that the GBDT and RF models shared optimal hyperparameter regions, indicating effective generalisation with minimal overfitting. XGBoost, however, showed signs of overfitting, making it less suitable for this dataset. 1D-CNN, and ResMLP models performed less effectively than the ensemble models, showing higher variance and weaker generalisation.
2. **GBDT Model Advantage:** GBDT emerged as the top-performing model with matrics of RMSE: 73.8, PCC: 0.93, and R^2: 0.87, excelling in yield stress prediction under radiation hardening conditions. The model identified Ta, W, and Cr as the most influential elements, with test temperature and irradiation dose were the most significant radiation parameters.
3. **Validation with Experimental Data:** GBDT's predictions were validated against experimental data for JLM-0, F82H, Eurofer97, and OPTIFER, demonstrating reliable performance across diverse irradiation and temperature conditions.
4. **Radiation Hardening Trends:** The study revealed that radiation hardening in reduced activation steels peaks around 315 °C and declines beyond 375 °C. The radiation dose effect showed increased hardening up to 20 dpa, a slight reduction between 20–35 dpa, and stabilisation beyond 35 dpa. While W and Cr enhanced hardening up to 375 °C, Cr had a more pronounced effect and Ta tended to mitigate hardening. These effects on radiation hardening are linked to changes in dislocation loops and precipitate behaviour.

This study underscores the transformative potential of machine learning in materials science, especially in predicting radiation hardening phenomena. Our findings provide a deeper understanding of radiation effects on RAFM steels, offering pathways to improved material performance in nuclear applications.

CRediT authorship contribution statement

Pengxin Wang: Writing – original draft, Visualization, Validation, Software, Methodology, Funding acquisition, Formal analysis, Data curation, Conceptualization. **Qing Tao:** Visualization, Resources, Project administration, Methodology. **Hongbiao Dong:** Project administration. **G.M. A. M. El-Fallah:** Writing – review & editing, Validation, Supervision, Project administration, Methodology, Investigation, Funding acquisition, Conceptualization.

Declaration of competing interest

The authors declare that they have no known competing financial interests or personal relationships that could have appeared to influence the work reported in this paper.

Acknowledgements

All authors gratefully acknowledge the support from Nanjing Iron & Steel United Co., Ltd. (NISCO), particularly for providing a PhD. Scholarship for this study.

Appendix A. Supplementary data

Supplementary data to this article can be found online at https://doi.org/10.1016/j.commatsci.2025.113773.

References

[1] N. Baluc, D.S. Gelles, S. Jitsukawa, A. Kimura, R.L. Klueh, G.R. Odette, B. van der Schaaf, J. Yu, Status of reduced activation ferritic/martensitic steel development, J. Nucl. Mater. 367–370 (2007) 33–41, https://doi.org/10.1016/j.jnucmat.2007.03.036.
[2] N. Baluc, R. Schäublin, P. Spätig, M. Victoria, On the potentiality of using ferritic/martensitic steels as structural materials for fusion reactors, Nucl. Fusion 44 (2004) 56–61, https://doi.org/10.1088/0029-5515/44/1/006.
[3] A. Bhattacharya, X. Chen, T. Graening, J.W. Geringer, J. Reed, J. Henry, L. Pilloni, D. Terentyev, A. Puype, T.S. Byun, Y. Katoh, M. Rieth, S.J. Zinkle, Irradiation hardening and ductility loss of Eurofer97 steel variants after neutron irradiation to ITER-TBM relevant conditions, Fusion Eng. Des. 173 (2021), https://doi.org/10.1016/j.fusengdes.2021.112935.
[4] A. Bhattacharya, S.J. Zinkle, J. Henry, S.M. Levine, P.D. Edmondson, M.R. Gilbert, H. Tanigawa, C.E. Kessel, Irradiation damage concurrent challenges with RAFM and ODS steels for fusion reactor first-wall/blanket: a review, J. Phys.: Energy 4 (2022), https://doi.org/10.1088/2515-7655/ac6f7f.
[5] S. Jitsukawa, K. Suzuki, N. Okubo, M. Ando, K. Shiba, Irradiation effects on reduced activation ferritic/martensitic steels—tensile, impact, fatigue properties and modelling, Nucl. Fusion 49 (2009), https://doi.org/10.1088/0029-5515/49/11/115006.
[6] A. Puype, L. Malerba, N. De Wispelaere, R. Petrov, J. Sietsma, Effect of processing on microstructural features and mechanical properties of a reduced activation ferritic/martensitic EUROFER steel grade, J. Nucl. Mater. 494 (2017) 1–9, https://doi.org/10.1016/j.jnucmat.2017.07.001.
[7] A.A.F. Tavassoli, E. Diegele, R. Lindau, N. Luzginova, H. Tanigawa, Current status and recent research achievements in ferritic/martensitic steels, J. Nucl. Mater. 455 (2014) 269–276, https://doi.org/10.1016/j.jnucmat.2014.06.017.
[8] S.J. Zinkle, J.L. Boutard, D.T. Hoelzer, A. Kimura, R. Lindau, G.R. Odette, M. Rieth, L. Tan, H. Tanigawa, Development of next generation tempered and ODS reduced activation ferritic/martensitic steels for fusion energy applications, Nucl. Fusion 57 (2017), https://doi.org/10.1088/1741-4326/57/9/092005.
[9] K. Linga Murty, Interstitial-Impurity Radiation-Defect Interactions in Ferritic Steels, JOM 37 (1985) 34–39, https://doi.org/10.1007/BF03258766.
[10] M.S. Wechsler, K.L. Murty, Impurity-defect interactions and radiation hardening and embrittlement in BCC metals, Metall. Trans. A 20 (1989) 2637–2649, https://doi.org/10.1007/BF02670157.
[11] W. Schule, R. Schulz, On radiation-induced structural changes in stainless steel alloys, J. Nucl. Mater. 104 (1981) 1367–1371, https://doi.org/10.1016/0022-3115(82)90790-5.
[12] D.S. Gelles, M.L. Hamilton, Effects of irradiation on low activation ferritic alloys, J. Nucl. Mater. 148 (1987) 272–278, https://doi.org/10.1016/0022-3115(87)90020-1.
[13] A. Kimura, M. Narui, T. Misawa, H. Matsui, A. Kohyama, Dependence of impact properties on irradiation temperature in reduced-activation martensitic steels, J. Nucl. Mater. 258–263 (1998) 1340–1344, https://doi.org/10.1016/S0022-3115(98)00321-3.
[14] O.V. Borodin, V.V. Bryk, V.N. Voyevodin, I.M. Neklyudov, V.K. Shamardin, Investigation of microstructure of ferritic-martensitic steels containing 9 and 13% Cr irradiated with fast neutrons, J. Nucl. Mater. 207 (1993) 295–302, https://doi.org/10.1016/0022-3115(93)90272-Z.
[15] Z. Tong, Y. Dai, The microstructure and tensile properties of ferritic/martensitic steels T91, Eurofer-97 and F82H irradiated up to 20dpa in STIP-III, J. Nucl. Mater. 398 (2010) 43–48, https://doi.org/10.1016/j.jnucmat.2009.10.008.
[16] T. Yamamoto, G.R. Odette, H. Kishimoto, J.-W. Rensman, P. Miao, On the effects of irradiation and helium on the yield stress changes and hardening and non-hardening embrittlement of ~8Cr tempered martensitic steels: Compilation and analysis of existing data, J. Nucl. Mater. 356 (2006) 27–49, https://doi.org/10.1016/j.jnucmat.2006.05.041.
[17] B.V.D. Schaaf, C. Petersen, Y. De Carlan, J.W. Rensman, E. Gaganidze, X. Averty, High dose, up to 80 dpa, mechanical properties of Eurofer 97, J. Nucl. Mater. 386–388 (2009) 236–240, https://doi.org/10.1016/j.jnucmat.2008.12.329.
[18] H. Tanigawa, R.L. Klueh, N. Hashimoto, M.A. Sokolov, Hardening mechanisms of reduced activation ferritic/martensitic steels irradiated at 300°C, J. Nucl. Mater. 386–388 (2009) 231–235, https://doi.org/10.1016/j.jnucmat.2008.12.094.
[19] D.S. Gelles, Microstructural examination of low activation ferritic steels following irradiation in ORR at 330 and 400 °C to ~10 dpa, J. Nucl. Mater. 329–333 (2004) 304–308, https://doi.org/10.1016/j.jnucmat.2004.04.049.
[20] P.P. Liu, M.Z. Zhao, Y.M. Zhu, J.W. Bai, F.R. Wan, Q. Zhan, Effects of carbide precipitate on the mechanical properties and irradiation behavior of the low activation martensitic steel, J. Alloys Compd. 579 (2013) 599–605, https://doi.org/10.1016/j.jallcom.2013.07.085.
[21] O.J. Weiß, E. Gaganidze, J. Aktaa, Quantitative characterization of microstructural defects in up to 32dpa neutron irradiated EUROFER97, J. Nucl. Mater. 426 (2012) 52–58, https://doi.org/10.1016/j.jnucmat.2012.03.027.
[22] L. Boulanger, Y. Serruys, Dislocation loops in Eurofer and a Fe–Cr alloy irradiated by ions at 350 and 550°C at 3dpa: Effect of dose rate, J. Nucl. Mater. 386–388 (2009) 441–444, https://doi.org/10.1016/j.jnucmat.2008.12.150.
[23] E. Materna-Morris, A. Möslang, R. Rolli, H.C. Schneider, Effect of helium on tensile properties and microstructure in 9%Cr–WVTa–steel after neutron irradiation up to 15dpa between 250 and 450°C, J. Nucl. Mater. 386–388 (2009) 422–425, https://doi.org/10.1016/j.jnucmat.2008.12.157.
[24] C. Dethloff, E. Gaganidze, J. Aktaa, Microstructural defects in EUROFER 97 after different neutron irradiation conditions, Nucl. Mater. Energy 9 (2016) 471–475, https://doi.org/10.1016/j.nme.2016.05.009.
[25] M. Klimenkov, E. Materna-Morris, A. Möslang, Characterization of radiation induced defects in EUROFER 97 after neutron irradiation, J. Nucl. Mater. 417 (2011) 124–126, https://doi.org/10.1016/j.jnucmat.2010.12.261.
[26] M. Klimenkov, U. Jäntsch, M. Rieth, A. Möslang, Correlation of microstructural and mechanical properties of neutron irradiated EUROFER97 steel, J. Nucl. Mater. 538 (2020), https://doi.org/10.1016/j.jnucmat.2020.152231.
[27] S.J. Zinkle, J.P. Blanchard, R.W. Callis, C.E. Kessel, R.J. Kurtz, P.J. Lee, K. A. McCarthy, N.B. Morley, F. Najmabadi, R.E. Nygren, G.R. Tynan, D.G. Whyte, R. S. Willms, B.D. Wirth, Fusion materials science and technology research opportunities now and during the ITER era, Fusion Eng. Des. 89 (2014) 1579–1585, https://doi.org/10.1016/j.fusengdes.2014.02.048.
[28] V.I. Dubinko, S.A. Kotrechko, V.F. Klepikov, Irradiation hardening of reactor pressure vessel steels due to the dislocation loop evolution, Radiat. Eff. Defects Solids 164 (2009) 647–655, https://doi.org/10.1080/10420150903115743.
[29] S. Kotrechko, V. Dubinko, N. Stetsenko, D. Terentyev, X. He, M. Sorokin, Temperature dependence of irradiation hardening due to dislocation loops and precipitates in RPV steels and model alloys, J. Nucl. Mater. 464 (2015) 6–15, https://doi.org/10.1016/j.jnucmat.2015.04.014.
[30] C. Deo, C. Tomé, R. Lebensohn, S. Maloy, Modeling and simulation of irradiation hardening in structural ferritic steels for advanced nuclear reactors, J. Nucl. Mater. 377 (2008) 136–140, https://doi.org/10.1016/j.jnucmat.2008.02.064.
[31] N. Naveen Kumar, P.V. Durgaprasad, B.K. Dutta, G.K. Dey, Modeling of radiation hardening in ferritic/martensitic steel using multi-scale approach, Comput. Mater. Sci 53 (2012) 258–267, https://doi.org/10.1016/j.commatsci.2011.08.035.
[32] Y. Zou, J. Qian, X. Wang, S. Li, Y. Li, Machine learning-assisted prediction and interpretation of electrochemical corrosion behavior in high-entropy alloys, Comput. Mater. Sci 244 (2024), https://doi.org/10.1016/j.commatsci.2024.113259.
[33] C. Herriott, A.D. Spear, Predicting microstructure-dependent mechanical properties in additively manufactured metals with machine- and deep-learning methods, Comput. Mater. Sci 175 (2020), https://doi.org/10.1016/j.commatsci.2020.109599.
[34] X. Huang, H. Wang, W. Xue, S. Xiang, H. Huang, L. Meng, G. Ma, A. Ullah, G. Zhang, Study on time-temperature-transformation diagrams of stainless steel using machine-learning approach, Comput. Mater. Sci 171 (2020), https://doi.org/10.1016/j.commatsci.2019.109282.
[35] J.A. Stewart, A.A. Kohnert, L. Capolungo, R. Dingreville, Design and analysis of forward and reverse models for predicting defect accumulation, defect energetics, and irradiation conditions, Comput. Mater. Sci 148 (2018) 272–285, https://doi.org/10.1016/j.commatsci.2018.02.048.
[36] P. Korotaev, A. Yanilkin, Neural networks for prediction of swelling in austenitic steels irradiated by fast neutrons, Comput. Mater. Sci 246 (2025), https://doi.org/10.1016/j.commatsci.2024.113408.
[37] R. Kemp, G.A. Cottrell, H.K.D.H. Bhadeshia, G.R. Odette, T. Yamamoto, H. Kishimoto, Neural-network analysis of irradiation hardening in low-activation steels, J. Nucl. Mater. 348 (2006) 311–328, https://doi.org/10.1016/j.jnucmat.2005.09.022.
[38] C.G. Windsor, G. Cottrell, R. Kemp, Prediction of yield stress in highly irradiated ferritic steels, Modell. Simul. Mater. Sci. Eng. 16 (2008) 025005, https://doi.org/10.1088/0965-0393/16/2/025005.

[39] Y. Zhou, S. Wang, R. Feng, Y. Xie, C. Fernandez, Multi-temperature capable enhanced bidirectional long short term memory-multilayer perceptron hybrid model for lithium-ion battery SOC estimation, Energy 312 (2024), https://doi.org/10.1016/j.energy.2024.133596.

[40] H. Yan, Q. Li, B. Yang, Y. Yang, Y. Wang, H. Zhang, Modeling and prediction method for young's moduli of Ti alloys based on residual muti-layer perceptron, JOM 77 (2024) 76–90, https://doi.org/10.1007/s11837-024-06942-3.

[41] G. Butterworth, Low activation structural materials for fusion, Fusion Eng. Des. 11 (1989) 231–244.

[42] T. Noda, F. Abe, H. Araki, M. Okada, Materials selection for reduced activation of fusion reactors, J. Nucl. Mater. 155 (1988) 581–584.

[43] A. Kimura, T. Morimura, M. Narui, H. Matsui, Irradiation hardening of reduced activation martensitic steels, J. Nucl. Mater. 233–237 (1996) 319–325, https://doi.org/10.1016/S0022-3115(96)00233-4.

[44] S. Knitel, P. Spätig, T. Yamamoto, H.P. Seifert, Y. Dai, G.R. Odette, Evolution of the tensile properties of the tempered martensitic steel Eurofer97 after spallation irradiation at SINQ, Nucl. Mater. Energy 17 (2018) 69–77, https://doi.org/10.1016/j.nme.2018.09.002.

[45] K. Shiba, A. Hishinuma, Low-temperature irradiation effects on tensile and Charpy properties of low-activation ferritic steels, J. Nucl. Mater. 283–287 (2000) 474–477, https://doi.org/10.1016/S0022-3115(00)00369-X.

[46] E. Lucon, R. Chaouadi, M. Decréton, Mechanical properties of the European reference RAFM steel (EUROFER97) before and after irradiation at 300 °C, J. Nucl. Mater. 329–333 (2004) 1078–1082, https://doi.org/10.1016/j.jnucmat.2004.04.023.

[47] E. Materna-Morris, A. Möslang, H.C. Schneider, Tensile and low cycle fatigue properties of EUROFER97-steel after 16.3dpa neutron irradiation at 523, 623 and 723K, J. Nucl. Mater. 442 (2013) S62–S66, https://doi.org/10.1016/j.jnucmat.2013.03.038.

[48] A. Alamo, J.L. Bertin, V.K. Shamardin, P. Wident, Mechanical properties of 9Cr martensitic steels and ODS-FeCr alloys after neutron irradiation at 325°C up to 42dpa, J. Nucl. Mater. 367–370 (2007) 54–59, https://doi.org/10.1016/j.jnucmat.2007.03.166.

[49] E. Gaganidze, C. Petersen, Post Irradiation Examination of RAF/M Steels After Fast Reactor Irradiation Up to 71 Dpa and < 340 ℃. 1 ed. KIT Scientific Publishing, Germany, 2011 Pages.

[50] J. Henry, X. Averty, A. Alamo, Tensile and impact properties of 9Cr tempered martensitic steels and ODS-FeCr alloys irradiated in a fast reactor at 325°C up to 78dpa, J. Nucl. Mater. 417 (2011) 99–103, https://doi.org/10.1016/j.jnucmat.2010.12.203.

[51] E. Gaganidze, H. Schneider, C. Petersen, J. Aktaa, A. Povstyanko, V. Prokhorov, R. Lindau, E. Materna-Morris, A. Möslang, E. Diegele, Mechanical properties of reduced activation ferritic/martensitic steels after high dose neutron irradiation. In Proc. of 22st IAEA Fusion Energy Conference, 2008.

[52] Y. Kohno, A. Kohyama, T. Hirose, M.L. Hamilton, M. Narui, Mechanical property changes of low activation ferritic/martensitic steels after neutron irradiation, J. Nucl. Mater. 271–272 (1999) 145–150, https://doi.org/10.1016/S0022-3115(98)00735-1.

[53] B. Gurovich, E. Kuleshova, Y. Shtrombakh, S. Fedotova, O. Zabusov, K. Prikhodko, D. Zhurko, Evolution of weld metals nanostructure and properties under irradiation and recovery annealing of VVER-type reactors, J. Nucl. Mater. 434 (2013) 72–84, https://doi.org/10.1016/j.jnucmat.2012.11.026.

[54] M. Johnson, M. Harned, S.B. Adisa, M. Moradi, M. Maughan, M.J. Swenson, Irradiation-induced microstructure and microchemistry effects on mechanical properties in ferritic-martensitic alloys, Materialia 20 (2021) 101228, https://doi.org/10.1016/j.mtla.2021.101228.

[55] Y. Luo, Y. Dong, X. Wang, H. Peng, D. Yan, T. Hu, S. Zhang, Q. Li, D. Wang, C. Xiao, In-situ TEM study of the effect of pre-existing dislocation on loop evolution in 508-III steel during Fe+ irradiation, J. Nucl. Mater. 559 (2022) 153420, https://doi.org/10.1016/j.jnucmat.2021.153420.

[56] W. Jiang, Y. Zhao, Y. Lu, Y. Wu, D. Frazer, D.P. Guillen, D.W. Gandy, J.P. Wharry, Comparison of PM-HIP to forged SA508 pressure vessel steel under high-dose neutron irradiation, J. Nucl. Mater. 594 (2024) 155018, https://doi.org/10.1016/j.jnucmat.2024.155018.

[57] A. Dubinko, N. Castin, D. Terentyev, G. Bonny, M.J. Konstantinović, Effect of Si–Ni–P on the emergence of dislocations loops in Fe–9Cr matrix under neutron irradiation: TEM study and OKMC modelling, J. Nucl. Mater. 540 (2020) 152395, https://doi.org/10.1016/j.jnucmat.2020.152395.

[58] M.J. Swenson, C.K. Dolph, J.P. Wharry, The effects of oxide evolution on mechanical properties in proton- and neutron-irradiated Fe-9%Cr ODS steel, J. Nucl. Mater. 479 (2016) 426–435, https://doi.org/10.1016/j.jnucmat.2016.07.022.

[59] F. Abe, T. Noda, H. Araki, M. Narui, H. Kayano, Irradiation hardening and ductility loss of a low-activation 9Cr-1V ferritic steel at low temperatures, J. Nucl. Mater. 166 (1989) 265–277, https://doi.org/10.1016/0022-3115(89)90223-7.

[60] E. Materna-Morris, H.C. Schneider, B. Daffener, R. Rolli, O. Romer, A. Moslang, Mechanical properties and structural analysis of martensitic low-activation alloys after neutron irradiation. In 20th IEEE/NPSS Symposium onFusion Engineering, 2003.

[61] M. Klimenkov, U. Jäntsch, M. Rieth, A. Möslang, Correlation of microstructural and mechanical properties of neutron irradiated EUROFER97 steel, J. Nucl. Mater. 538 (2020) 152231, https://doi.org/10.1016/j.jnucmat.2020.152231.

[62] Y. Kohno, A. Kohyama, D.S. Gelles, K. Asakura, Radiation induced microstructural evolution in ferritic/martensitic steels, Mater. Trans. JIM 34 (1993) 1018–1026, https://doi.org/10.2320/matertrans1989.34.1018.

[63] S. Hiwatashi, Y. Kohno, K. Asakura, A. Kohyama, Microstructural developments in Fe-Cr-W low activation ferritic steels under dual beam charged particle irradiation, J. Nucl. Mater. 179–181 (1991) 709–713, https://doi.org/10.1016/0022-3115(91)90187-C.

[64] P. Fernández, A.M. Lancha, J. Lapeña, R. Lindau, M. Rieth, M. Schirra, Creep strength of reduced activation ferritic/martensitic steel Eurofer'97, Fusion Eng. Des. 75–79 (2005) 1003–1008, https://doi.org/10.1016/j.fusengdes.2005.06.085.

[65] S. Yin, L. Yang, Y. Liu, R. Yang, Y. Wang, F. Zhao, Stabilities of the precipitates in CLAM steel during 30,000 h thermal aging, J. Nucl. Mater. 567 (2022) 153805, https://doi.org/10.1016/j.jnucmat.2022.153805.

[66] A. Fedoseeva, I. Nikitin, N. Dudova, R. Kaibyshev, Coarsening of Laves phase and creep behaviour of a Re-containing 10% Cr-3% Co-3% W steel, Mater. Sci. Eng. A 812 (2021) 141137, https://doi.org/10.1016/j.msea.2021.141137.

[67] X. Jia, Y. Dai, M. Victoria, The impact of irradiation temperature on the microstructure of F82H martensitic/ferritic steel irradiated in a proton and neutron mixed spectrum, J. Nucl. Mater. 305 (2002) 1–7.

[68] X. Jia, Y. Dai, Microstructure in martensitic steels T91 and F82H after irradiation in SINQ Target-3, J. Nucl. Mater. 318 (2003) 207–214.

[69] J.P. Sanhueza, D. Rojas, J. García, M.F. Melendrez, E. Toledo, C. Montalba, M. I. Alvarado, A.F. Jaramillo, Computational modeling of the effect of B and W in the phase transformation of M23C6 carbides in 9 to 12 pct Cr martensitic/ferritic steels, Mater. Res. Express 6 (2019) 1165d3, https://doi.org/10.1088/2053-1591/ab500c.

[70] R.S. Nelson, J.A. Hudson, D.J. Mazey, The stability of precipitates in an irradiation environment, J. Nucl. Mater. 44 (1972) 318–330, https://doi.org/10.1016/0022-3115(72)90043-8.

[71] H. Tanigawa, H. Sakasegawa, H. Ogiwara, H. Kishimoto, A. Kohyama, Radiation induced phase instability of precipitates in reduced-activation ferritic/martensitic steels, J. Nucl. Mater. 367–370 (2007) 132–136, https://doi.org/10.1016/j.jnucmat.2007.03.155.

[72] L. Tan, T.S. Byun, Y. Katoh, L.L. Snead, Stability of MX-type strengthening nanoprecipitates in ferritic steels under thermal aging, stress and ion irradiation, Acta Mater. 71 (2014) 11–19, https://doi.org/10.1016/j.actamat.2014.03.015.

[73] T.R. Allen, G.S. Was. Radiation-enhanced diffusion and radiation-induced segregation. in Radiation Effects in Solids. 2007. Dordrecht: Springer.

[74] R. Sizmann, The effect of radiation upon diffusion in metals, J. Nucl. Mater. 69–70 (1978) 386–412, https://doi.org/10.1016/0022-3115(78)90256-8.

[75] J.P. Wharry, G.S. Was, The mechanism of radiation-induced segregation in ferritic–martensitic alloys, Acta Mater. 65 (2014) 42–55, https://doi.org/10.1016/j.actamat.2013.09.049.

[76] R.L. Klueh, Reduced-activation bainitic and martensitic steels for nuclear fusion applications, Curr. Opin. Solid State Mater. Sci. 8 (2004) 239–250, https://doi.org/10.1016/j.cossms.2004.09.004.

[77] S. Rogozhkin, A. Nikitin, N. Orlov, A. Bogachev, O. Korchuganova, A. Aleev, A. Zaluzhnyi, T. Kulevoy, R. Lindau, A. Möslang, P. Vladimirov, Evolution of microstructure in advanced ferritic-martensitic steels under irradiation: the origin of low temperature radiation embrittlement, MRS Adv. 2 (2017) 1143–1155, https://doi.org/10.1557/adv.2016.657.

[78] R. Ravikirana, S. Mythili, S. Raju, T.J. Saroja, E. Rajendrakumar, Influence of W and Ta content on microstructural characteristics in heat treated 9Cr-reduced activation ferritic/martensitic steels, Mater. Charact. 84 (2013) 196–204, https://doi.org/10.1016/j.matchar.2013.08.003.